# Point Defects and Related Excess Electrons in the Dielectric Prole of the Reduced TiO 2 (110) Surface

Jingfeng Li, Stéphane Chenot, Jacques Jupille, Remi Lazzari

## To cite this version:

Jingfeng Li, Stéphane Chenot, Jacques Jupille, Remi Lazzari. Point Defects and Related Excess Electrons in the Dielectric Prole of the Reduced TiO 2 (110) Surface. Journal of Physical Chemistry C, 2021, 125 (30), pp.16652-16663. 10.1021/acs.jpcc.1c01796 . hal-03370035

HAL Id: hal-03370035
https://hal.science/hal-03370035v1

Submitted on 7 Oct 2021

# Point Defects and Related Excess Electrons in the Dielectric Profile of the Reduced $TiO_2$(110) Surface

Jingfeng Li, Stéphane Chenot, Jacques Jupille, and Rémi Lazzari*

*CNRS, Sorbonne Université, Institut des NanoSciences de Paris, UMR 7588, 4 Place Jussieu, F-75005 Paris, France*

E-mail: remi.lazzari@insp.jussieu.fr

## Abstract

The dielectric behavior of the reduced $TiO_2$(110) rutile surface has been explored by High-Resolution Electron Energy Loss Spectroscopy as a function of oxygen exposure, temperature and crystal orientation (dielectric anisotropy) to highlight at once the electrical transport of excess electrons and the associated band gap states (BGS), and to establish a dielectric model that encompasses the surface region as a whole. Never explored distribution profiles were determined in two steps: charge carriers and then defects themselves. Firstly, surface and bulk carrier excitations were directly evidenced by the temperature-dependent broadening of the quasi-elastic peak and changes in loss features, which legitimates fits via a previous dielectric model accounting for phonons, interband transitions, plasmon excitations and BGS. The density profile of excess electrons, involving a dead zone, a rich subsurface and a lower bulk concentration was quantitatively optimized. Surface and bulk concentrations, donor and Fermi levels match tabulated values. In a second step, three types of defects were distinguished *i.e.* $O_b$(vac), surface $Ti_{int}$ and bulk $Ti_{int}$ thanks to changes in surface and bulk plasmon and BGS strengths upon oxygen exposure of the reduced surface. Each of them exhibits a specific behavior. While the surface conductivity requires the presence of $O_b$(vac), both $O_b$(vac) and surface $Ti_{int}$ participate in surface reactions and all three species contribute to band bending which evidences that defects, alone or by cross influences, shape the location and the properties of excess electrons. Making it crucial to take into account the fact, often overlooked, that excess electrons do not behave independently of their source, the finding suggests studying defects taken individually or within controlled combinations.

## 1 Introduction

Reduced non-stoichiometric rutile $TiO_2$(110) is a n-type semiconductor of which main point defects, surface oxygen vacancies $O_b$(vac) and titanium interstitials $Ti_{int}$ (Figure 1), dominate electronic properties.[1–4] The excess electrons they generate have a strong polaronic character; they are located on regular Ti lattice sites on which they populate Ti 3d-derived states lying in the band gap (BGS) at 0.8-1 eV below the Fermi level,[1–7] as evidenced by photoemission[8–12] and various spectroscopies.[13–16] The experimental finding of a high density of excess electrons in subsurface,[10,14,17] which relies on the surface electrostatic potential of the oxide, is supported by *ab initio* methods (DFT+U, hybrid functional, PBE+U[18–24]) that also predict a localization of excess electrons in deep states in agreement with spectroscopic measurements.

This configuration is all the more general as injection of electrons[10] or n-doping with hydrogen,[25,26] aliovalent cations or anions[16] lead to charge distributions similar to those produced by stoichiometry defects. The actual involvement of point defects in the physics and chemistry of titania surfaces became highly controversial in the last fifteen years.[11,27–29] Long been associated with $O_b$(vac),[8] surface BGS were related to $Ti_{int}$ on the basis of the chemistry of the surface hydroxyl groups ($O_bH$) while the ability $O_b$(vac) and $O_bH$ to participate in the Ti 3d defect states was questioned.[27] Conversely, in support of the classic model, the BGS intensity was correlated with the density of $O_b$(vac).[11] Resolving the controversy requires isolating the two species, which has so far been prevented by the similarity of the spectroscopic signatures of the excess electrons associated with them[14,18,22,30] and the inability to directly identify $Ti_{int}$.[31] While the debate is fueled by surface chemistry, surface physics lacks readability.

The issue prompted us to develop innovative methods[14,32] to isolate the $TiO_2$(110) point defects and to revisit the modeling of High-Resolution Electron Energy Loss spectra (HREELS) of titania on the basis of the dielectric theory.[33–38] As a powerful probe for surface excitations, HREELS parallels optics while covering a wider energy range with a variable surface/bulk sensitivity.[39] Also, it has a higher probing depth than ultraviolet photoemission.[14] Isolated $O_b$(vac) were prepared by electron stimulated desorption[40] (ESD) while $Ti_{int}$-enriched subsurface was obtained by soft annealing of the very first surface layers by a hot filament.[14] (By the way, we ensured that the ESD filament used to generate $O_b$(vac) does not cause diffusion of $Ti_{int}$[14]). Although $O_2$ heals both $O_b$(vac) via a direct reaction and $Ti_{int}$ via charge transfer,[15,27] $O_b$(vac) were discriminated by $H_2O$ adsorption followed by ESD of $H^+$[40,41] ($H_2O$/ESD), a process that does not affect $Ti_{int}$.[14] A first important conclusion was that each kind of point defects, being alone, produce excess electrons,[14] which removes doubt about the contribution of $O_b$(vac) to Ti 3d defect states.[27]

Regarding characterization of charge transport by dielectric modeling, a drawback comes from the high value of the static dielectric constant [$\epsilon_{\parallel}(0) = 153$ and $\epsilon_{\perp}(0) = 84.7$[42,43]] that stem from the severe longitudinal/transverse splitting of the phonon modes. Combined with the effective mass $m^* = 8 - 10$,[44–46] and despite a strong carrier concentration $n$,[44] this yields a surface plasmon energy $\omega_{sp} \propto \frac{n}{m^* \sqrt{1+\epsilon(0)}}$ two orders of magnitude lower than that of classical semiconductors,[33] which results in a hardly detectable plasmon excitation at the foot of the elastic peak and explains why HREELS failed to deal with transport properties in $TiO_2$.[38,47,48] Contributions of phonons, interband transitions and defect-related excitations (plasmon and BGS) [49] were defined to reinvestigate the case via the semiclassical dielectric theory of EELS. Fits demonstrate (i) distinct surface and bulk transport properties and (ii) a dual behavior of excess electrons (BGS oscillator strength clearly correlates with plasmon frequency[32]) which, due to their polaronic behavior, appear as either deeply bound or highly mobile depending on excitation frequency.

So far, we have identified $O_b$(vac) and $Ti_{int}$, plasmons and BGS under the implicit (and common) assumption that defects all produce similar excess electrons and do not specifically affect their properties, which is highly debatable. HREELS is a relevant method for discussing the issue. Since it reconciles transport and spectroscopy, it can distinguish the different entities that contribute to dielectric behavior, provided that it goes beyond the limit of previous work which characterized plasmon, phonon and BGS excitations by means of a single fit.[32,49] We require the direct knowledge of the individual fingerprints of each entity contributing to the electronic status of the reduced $TiO_2$ surface [R-$TiO_2$(110)] with a particular focus on the vividly debated charge carrier excitations and $Ti_{int}$. We plan to meet the challenge by a step-by-step loss analysis of R-$TiO_2$(110) exposed to oxygen which, because of the specificities of its reactivity, is expected to allow a cartography of the defective titania surface. Our objectives are: (i) the direct demonstration of the existence of plasmonic fingerprints of the surface and bulk charge carriers in loss spectra and, then, the quantitative determination of charge carrier profile, including anisotropy; (ii) the determination of the distribution of the various types of defects in the surface region in relation to the charge carrier profile; (iii) the exploration of combined properties of defects and carriers (n-type character of the oxide, transport properties and band bending prior to (iv) discussion.

# 2 Methods

Experiments have been performed in a ultra-high vacuum (UHV) vessel[50] including a preparation chamber (base pressure $3.10^{-10}$ mbar) and an analysis chamber ($< 5.10^{-11}$ mbar) equipped, respectively, with a four grid LEED (Low Energy Electron Diffraction)-Auger and an high resolution electron energy loss spectrometer (HREELS) operated in reflection (LK-2000[51,52]). Vibrational spectra have been acquired in HREELS (EELS) mode with a beam energy of $E_I = 7.5$ eV ($E_I = 38$ eV), a step width of $\Delta\hbar\omega = 0.3 - 0.6$ meV ($\Delta\hbar\omega = 1.8 - 3.6$ meV), a Full-Width at Half-Maximum (FWHM) of the quasi-elastic peak (QEP) of $\text{FWHM}_H = 9 - 13$ meV ($\text{FWHM}_L \simeq 50$ meV) and a the corresponding counting rate on QEP of $I_H^{qep} = 1 - 8 \times 10^5$ counts.s$^{-1}$ ($I_L^{qep} = 2 - 4 \times 10^6$ counts.s$^{-1}$). Although the Ti 3p-related Auger transition at 34 eV entails the formation of $O_b$(vac),[14,40,53] beam damage due to the use of $E_I = 38$ eV in EELS has never been observed owing to the small incident current (< 10 nA) and the weak cross section of the phenomenon.[53,54] Spectra were stable for hours. $O_b$(vac) could only be created by a much higher electron bombardment with an ancillary electron gun.[14] Measurements were performed in specular condition at an incident angle of $\Theta_I = 60°$ (Figure 1). When the scattering plane is normal to the c-axis (*i.e.* to the bridging oxygen rows), the effective dielectric function used in simulations and on which depends the loss function is $\xi(\omega) = \epsilon_\perp(\omega)$,[49,55] where $\epsilon_\perp(\omega)$ is the dielectric tensor component perpendicular to c-axis. For scattering plane parallel to c-axis, both parallel and perpendicular components are involved in $\xi(\omega) = \sqrt{\epsilon_\perp(\omega)\epsilon_\parallel(\omega)}$.[49,55]

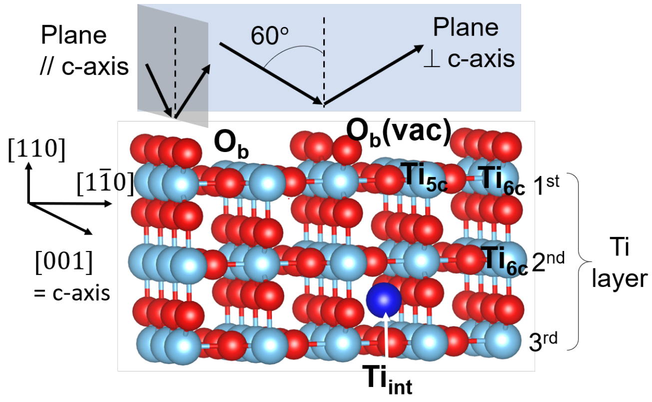

Figure 1: Ball model of the $TiO_2(110)$ surface showing the EELS scattering geometry relative to crystallographic directions. Blue (red) balls stand for Ti (O) atoms. The main point defects, oxygen vacancy $O_b$(vac) on bridging oxygen $O_b$ row and interstitial titanium $Ti_{int}$ are shown along with the 5-fold ($Ti_{5c}$) and 6-fold ($Ti_{6c}$) coordinated surface Ti atoms. In what follows, Ti atoms that are below those atoms are labelled $Ti_{5c} - 1^{st}$ ($Ti_{6c} - 1^{st}$), $2^{nd}$ and $3^{rd}$, irrespective of the actual coordination number they have in the layer in which they are localized.

To favor a good thermal contact,[14] the double-side polished $TiO_2(110)$ crystal (Mateck GmbH[56]) has been firmly clamped on a Ta plate with an Au foil inserted in between. In the EELS spectrometer, the sample could be cooled down to $T \simeq 100$ K by circulating liquid nitrogen, radiatively heated up to $T \simeq 500$ K and exposed to high purity gases through a leak-valve. Temperature was monitored by a thermocouple clamped on the copper head of the sample manipulator and cross-checked from Boltzmann ratio of gain/loss at phonon energies.[33,39] Care was taken to keep the same apparatus lens settings[33,57] and resolution function throughout gas exposures despite the decrease in counting rate due to $O_2$ adsorption on the electron gun filament. The exposure is given in Langmuir (L), 1 L corresponding to $10^{-6}$ torr during one second. The surface has been prepared by cycles of sputtering with $Ar^+$ ions at 1 keV (10 mins) followed by annealing under UHV at $T \simeq 1100$ K by electron bombardment of the metallic back plate (20 mins). After several cycles, the reduced R-$TiO_2$(110) crystal turned dark blue. The surface was free of contaminants as checked by Auger spectroscopy, sample reflectivity in EELS and lack of CH-stretching modes. A sharp $(1 \times 1)$ LEED pattern was routinely achieved. No trace of $(1 \times 2)$ reconstruction could be observed.

# 3 Results

The sputtered/annealed R-$TiO_2$(110) studied herein is a good case study since, as it involves both $Ti_{int}$ and $O_b$(vac), it is anticipated to be representative of most defective configurations encountered in reduced rutile.

## 3.1 Surface and bulk carriers in rutile

The dielectric model predicts three main evolutions in $TiO_2$(110) loss spectra upon reduction:[49,50] (i) plasmon excitations induce a temperature-dependent broadening of the QEP; this effect is crucial since, due to the plasmons alone, it unambiguously demonstrates their existence; (ii) BGS and plasmons decrease phonon/elastic intensity ratio; (iii) the plasmon screening blueshifts the phonon energy otherwise redshifted by the occurrence of BGS. Testing the validity of these predictions requires highlighting the signatures of charge carriers and their changes as a function of the reduction state of the oxide. This has been done herein by $O_2$ exposure of R-$TiO_2$(110) at 100 K and 300 K.

### 3.1.1 Featuring carrier excitations in $TiO_2$(110) loss spectra

Loss spectra (Figure 2) have been collected with the scattering plane (Figure 1) either normal (Figure 2-a,b,c,d) or parallel to c-axis (Figure 2-e,f). Losses include QEP, surface phonons, band gap, BGS and interband transitions (Figure 2-a,b). The BGS is associated to a 0.8 eV loss that corresponds to the optical absorption by a polaronic trapping state, *i.e.* a quasi-particle made of an electron and the accompanying phonon cloud due to lattice distortions.[49,58] To cancel the impact of $O_2$ exposure on the counting rate, spectra were normalized to the intense and bulk sensitive[14,49] phonon at $\hbar\omega_{sph,3} = 95$ meV (Figure 2). BGS evolutions at 100 and 300 K (scattering plane normal to c-axis) are compared in the inset of Figure 2-d. The steep decrease of BGS at 100 K stems from long-living physisorbed $O_2$ molecules that diffuse until they adsorb on $O_b$(vac), leading to a sticking coefficient of $O_2$ close to unity.[58] The slower filling of $O_b$(vac) at 300 K indicates a shorter lifetime of $O_2$ prior to dissociation.[13,54] However, similar BGS intensities after $\simeq 25$ L at 100 K and 3000 L at 300 K (inset of Figure 2-d) suggest similar adsorption sites although mechanisms differ. Up to 300 K, in the absence of diffusion of $Ti_{int}$, $O_2$ adsorption only scavenges subsurface excess charges; residual BGS (Figure 2-b,d,f) are attributed to bulk $Ti_{int}$ not affected by $O_2$ exposure.[14]

In line with the first prediction of dielectric theory,[49] the extra-broadening of 2.5 meV of the oxide QEP (Figure 3-a) relative to that of Pt(111) suggests a plasmon excitation of a few tens of meV;[49,50] its existence is unambiguously confirmed by the temperature-dependent QEP broadening observed between 95 K and 420 K (Figure 3-b). Indeed, no broadening is expected for stoichiometric titania or BGS alone;[49,50] moreover, any assignment of the QEP asymmetry to a combination $\hbar\omega_{sph,2} - \hbar\omega_{sph,1} \simeq 10$ meV of surface phonons $\hbar\omega_{sph,1,2,3} \simeq 45; 55; 95$ meV is ruled out since, predicted to be of poor intensity,[49] such a combination should be insensitive to adsorption and should disappear at $T = 100$ K contrary to observation (Figure 3-c,d). By comparison to Figure 5 of Reference 49, the QEP broadening substantiates the existence of Drude-type carriers with a concentration normalized to effective mass of $n/m^* \simeq 10^{19}$ cm$^{-3}$ and a mild plasmon damping. Carrier excitations are further evidenced by the enhancement upon $O_2$ exposure of the high energy asymmetry of the QEP that replicates at the foot of $\omega_{sph,3}$ (Figure 2-a and Figure 3-d,e). Assuming that healing the subsurface excess charges by $O_2$ increases the HREELS probing depth, the asymmetry is assigned to bulk carriers (see Figure 13 of Reference 49). Lower energy due to lower carrier concentration (by 4 to 5) at 100 K compared to 300 K[32] explain the relatively modest asymmetry and QEP/phonon changes observed at 100 K (Figure 3-d,e).

The decrease in the QEP/phonon ratio upon $O_2$ exposure (Figure 2) demonstrates the validity of the second prediction since, by healing BGS and plasmons, $O_2$ adsorption entails an increase in phonon intensity. (Such a variation cannot result from oxygen adsorption that only affects the extreme surface while phononic excitations extend deep inward the solid.[14,49])

The third prediction is that plasmon and BGS excitations taken independently affect the position and profile of phonon lines.[49] The effect is directly revealed at the onset of a native crystal preparation as $\omega_{sph,3}$ reaches the final energy of 95 meV (Figure 4) after a few sputtering-annealing cycles while the substrate acquires a light blue color. In a more general approach, intrinsic phonon line profiles have been analyzed by removing multiple excitation and combination modes via Fourier transform[59] from a loss spectrum recorded on R-$TiO_2$(110) at 98 K (Figure 5). Resolution has then been enhanced via a semi-blind Lucy-Richardson algorithm,[50] but only down to a QEP FWHM$_a$ of 2.2 meV to prevent noise amplification. (Incidentally, the FWHM found for the apparatus function equals within 0.2 meV that of Pt(111).) The lorentzian profiles of phonon peaks are then recovered as expected from oscillator behavior[33,49] only if the QEP asymmetry is treated as a signal in the deconvolution process instead of being included in the apparatus response function (Figure 5). The lorentzian fits match the relative area and FWHMs of phonon loss peaks calculated from tabulated loss function of stoichiometric rutile[43,49] (Figure 5); however, the phonon frequencies are shifted by fractions of meV as a result of the combination of opposite screenings of BGS and carrier excitations,[49] which proves the existence of both in line with the dual polaronic behavior of excess electrons.[32,49]

Finally, in agreement with the dielectric model, QEP profile and QEP/phonon ratio much depend on the scattering geometry (Figure 2-a,c,e) but not BGS (Figure 2-b,d,f). The interband transitions are orientation-dependent (Figure 2-d,f), an unexpected phenomenon (see supporting information (SI) of Reference 49 vs Figure S1-b,d) likely due to the breakdown of the dielectric assumption caused by the surface sensitivity at the energies considered.[49] In passing, in either scattering geometry, the surface band gap derived from EELS (probing depth below $\simeq 10$ Å, SI of Reference 14) is close to the bulk value ($\simeq 3.1$ eV at 300 K,[60] Figure 1-c of Reference 32) despite a reduced coordination. In this respect, the rather covalent $TiO_2$ contrasts with the strongly ionic MgO, for which the Madelung field leads to different surface and bulk band splitting.[61,62]

Therefore, plasmons excitations involved in changes in phonon energy, line shape and QEP/phonon ratio upon reduction of the oxide are also directly evidenced by the QEP broadening. Moreover, the visualization of the contribution of the bulk carriers at the foot of the QEP demonstrates the ability of loss analysis to discriminate surface and bulk excitations and provides a reliable basis for the quantitative modeling presented in the following sections.

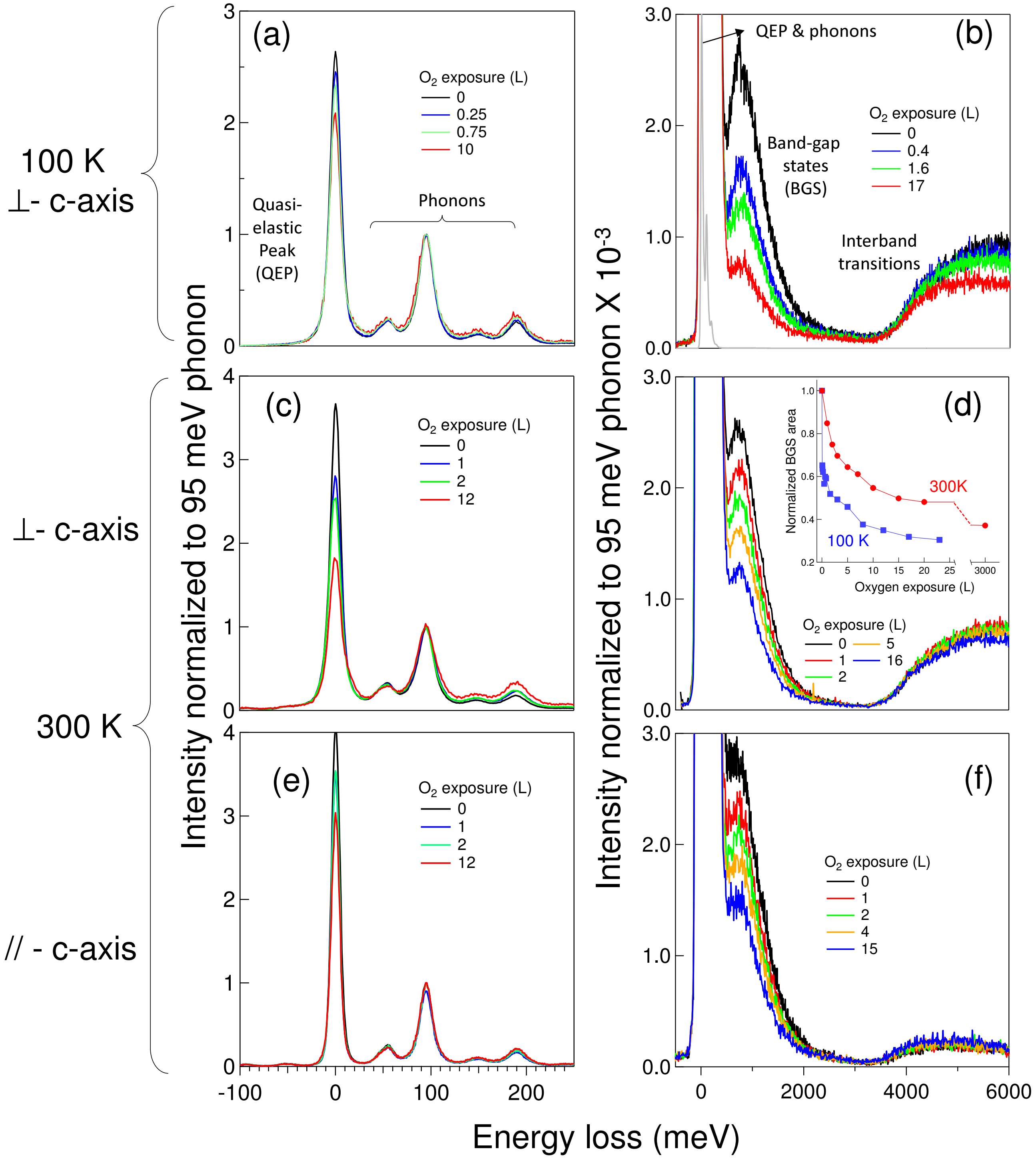

Figure 2: Effect of $O_2$ exposure on loss spectra of R-$TiO_2$(110): (a) HREELS ($E_I = 7.5$ eV; FWHM of QEP of 13 meV) and (b) EELS ($E_I = 38$ eV; FWHM of QEP of 50 meV) data acquired at 100 K for an incident electron beam perpendicular to c-axis (Figure 1) of $TiO_2$; (c)(d) at 300 K, same settings; (e)(f) at 300 K, same settings but with a beam parallel to c-axis. The inset in Figure d shows the evolutions of the integrated BGS intensities at 100 and 300 K for an incident electron beam perpendicular to c-axis.

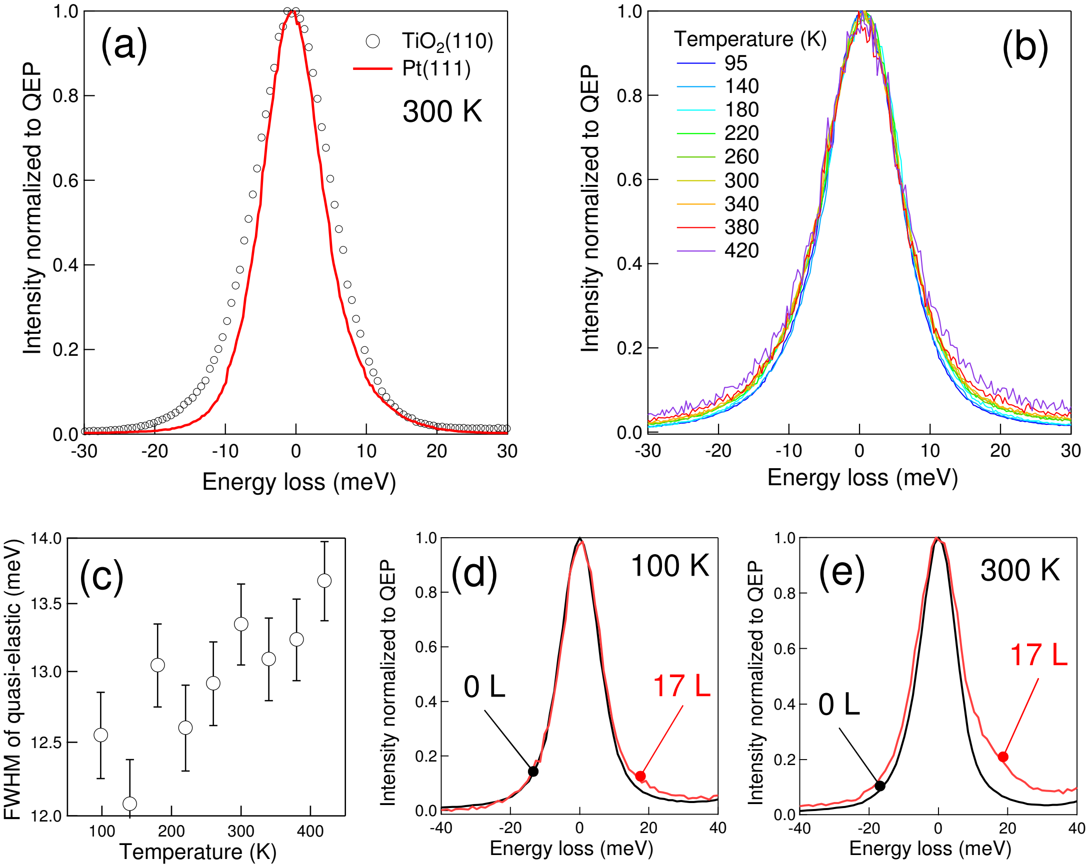

Figure 3: QEP profile and width of R-TiO$_2$(110): (a) comparison to that of Pt(111) (FWHM of 10 meV) by using similar spectrometer settings, (b) its evolution in the 95-420 K temperature range (only the thermal drift of the sample position was mechanically compensated) and (c) the corresponding FWHM; (d) and (e) change in QEP line shape upon O$_2$ exposure of R-TiO$_2$(110) at 100 and 300 K, respectively.

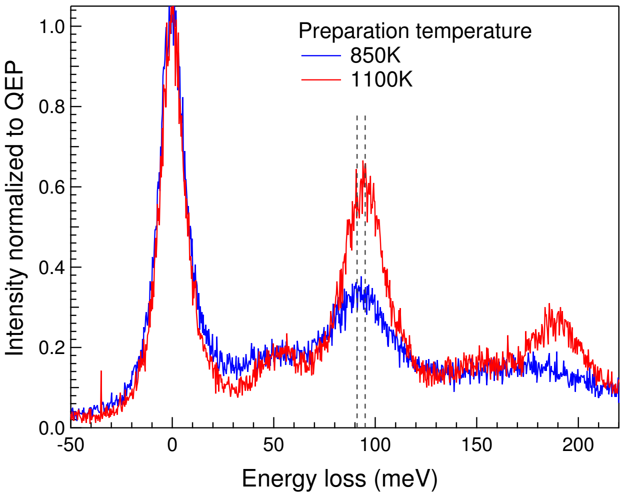

Figure 4: Phonon spectra of a $TiO_2(110)$ sample at the earliest stage of preparation. The counting statistics of a few hundred counts reflects a poor surface quality. A slight phonon shift due to screening is observed after a few sputtering-annealing cycles, the obtained $\omega_{sph,3}$ energy of 95 meV remaining constant even in heavily reduced samples.

### 3.1.2 The profile of the dielectric function of excess electrons used in fits

Loss data are fitted by using the following expression of the dielectric function[32,49] (see Section S1 of supporting information):

$$\epsilon_{TiO_2}(\omega) = \epsilon_{Ph}(\omega)+\epsilon_{Ib}(\omega)+\epsilon_{gs}(\omega)+\epsilon_{Pl}(\omega), \quad (1)$$

which involves phonons $\epsilon_{Ph}(\omega)$ and interband transitions $\epsilon_{Ib}(\omega)$ terms taken from tabulated optical data.[43,63] BGS contributions $\epsilon_{gs}(\omega)$ are accounted for by an oscillator of strength $\Omega_{gs}$, frequency $\omega_{gs}$ and damping $\Gamma_{gs}$ while transport $\epsilon_{Pl}(\omega)$ is featured by a Drude model with a plasmon frequency $\omega_P$ and damping $\Gamma_P$. The $S, B$ subscript indexes used hereafter for such quantities stand for surface and bulk quantities as defined below. Carrier density $n$ and mobility $\mu$ are related to $\omega_P = \sqrt{ne^2/m_e m^* \epsilon_0}$ and $\Gamma_P = 2\pi e/m_e m^* \mu$ where $m^*$ is the electron effective mass and $(e, m_e, \epsilon_0)$ have their usual meanings.

Off-specular EELS[14] shows that fits require a carrier profile involving a 2.5 Å thick depleted surface layer, a layer of thickness $t_S$ encompassing subsurface excess electrons and a deep bulk contribution attributed to $Ti_{int}$[14] modeled by a constant concentration (Figure 6-a). The fitting strategy is to extract bulk parameters from EELS after quenching surface excess electrons by $O_2$ ($\gtrsim$ 10 L), thus assuming $\Omega_{gs,S} = 0$, prior to using these to analyze surface excitations via HREELS spectra of the as-prepared R-$TiO_2(110)$ (0 L $O_2$).[32] However, quantitative analysis requires to determine $t_S$, here assumed to involve an integer number of unit cells along the [110] direction (6.5 Å, *i.e.* three atomic Ti layers). Fits performed on HREELS (0 L $O_2$) and EELS (20 L) much worsen for $t_S$ higher than 26 Å are definitively better for 6.5-13 Å (Figure 6-b,c). However, the spatial extension of $t_S$ might depend on the nature of the excitation. To explore the case, fits were done at a fixed thickness $t_{BGS} = 6.5 - 13$ Å for BGS (known enrichment of the subsurface[10,14,17,20,32]) and a thickness $t_S$ for transport. Inconsistent decreasing $t_S$ values from 40 Å to nearly zero were obtained between 0 and 4 L. But whatever $t_S$, the product $t_S \omega_{P,S}^2 \propto n_S/m^*$ found constant (inset of Figure 6-a) indicates a constant density $n_S \simeq 10^{14}$ cm$^{-2}$ of surface carriers on the native surface, assuming the release of two electrons per defect, an effective mass $m^*_\perp \simeq 10$ and an anisotropy $m^*_\perp/m^*_\parallel = 0.5$. In what follows, fits are systematically performed for $t_S = 6.5$ Å, in agreement with the experimental[10,17] and theoretical[20] findings that excess charges mainly populate the three first $TiO_2(110)$ surface layers.

Fits were performed for loss spectra of Figure 2, recorded perpendicular (at 100 K, Figure S1, and 300 K, Figure 1 of Reference 32) and parallel to c-axis (at 300 K, Figure S1). Knowing the perpendicular parameters,[49] the above methodology was used to examine the data collected parallel to c-axis, the bulk analysis preceding that of the surface. Surface and bulk parameters in the two scattering geometries are gathered in Table S1. Since the carrier density does not depend on direction (*i.e.* $n_{B,\parallel} = n_{B,\perp}$), the anisotropy of the bulk

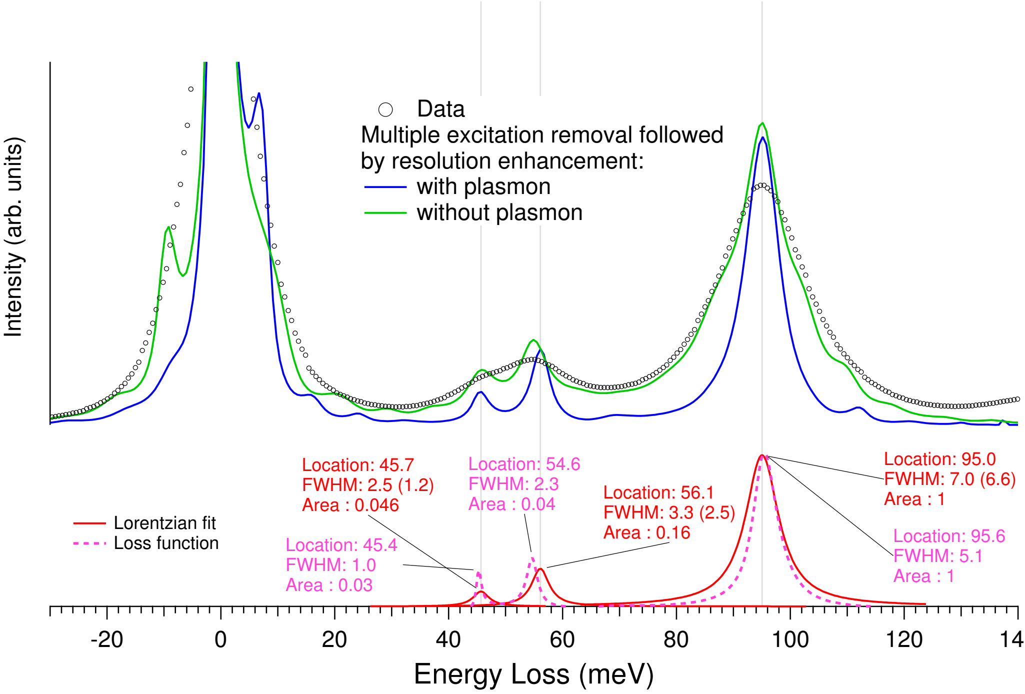

Figure 5: Effect of removal of multiple excitation and combination modes followed by resolution enhancement using a semi-blind Lucy-Richardson algorithm (see text) on an HREELS spectrum recorded at 98 K in a geometry normal to c-axis (circles). The QEP shoulder is treated as an actual excitation (blue curve) or included in the resolution function (green curve) in Fourier-based treatment.[59] Lorentzian fits (red curve) of the main phonon peaks of the blue curve are compared to the phonon loss function $\mathrm{Im}[1/1+\epsilon_{Ph,\perp}(\omega)]$ (pink dotted curve); $\epsilon_{Ph,\perp}(\omega)$ is the tabulated dielectric contribution associated to phonons only.[43] Values of peak positions, FWHMs and areas relative to the three surface phonons are given in figure. The experimental value $\mathrm{FWHM}_{s,ph}$ given in parenthesis was obtained by removing the remaining elastic peak $\mathrm{FWHM}_a = 2.2$ meV through $\mathrm{FWHM}^2_{s,ph} = \mathrm{FWHM}^2 - \mathrm{FWHM}^2_a$.

plasma frequency is related to that of the effective mass $m^*_\perp/m^*_\parallel = 3.4 \pm 2.4$, in reasonable agreement with transport measurements ($m^*_\perp/m^*_\parallel = 4.3 \pm 2.4$)[44] and terahertz optical spectroscopy ($m^*_\perp/m^*_\parallel = 7.5$).[46] The anisotropy of the effective mass $m^*_\perp/m^*_\parallel = 0.5 \pm 0.5$ of surface carriers, never determined to date, is much less marked than in bulk. Their much lower mobility suggests a confinement by a different electrostatic potential.

The fair account of loss spectra (Figure S1) raises the confidence about the chosen carrier profile and demonstrates the robustness of the dielectric approach. In the next section, the variations as a function of $O_2$ exposure of the surface and bulk dielectric parameters (Figure 7) allow, over the entire depth of the surface region, to grasp most of the physics of excess charges and, in parallel, to relate the excess charges to the defects which generate them.

## 3.2 The role of the different types of defects in the n-type character of rutile

### 3.2.1 Concomitant contributions of $O_b$(vac) and $Ti_{int}$ to the surface region

At 100 K, the complete cancellation of the plasmon strength after only 1 L $O_2$ (Figure 7-a) while BGS are still observed (Figure 7-b) indicates two different regimes. Firstly, the elimination of surface plasmons by an $O_2$ exposure similar to that required to heal "pure" $O_b$(vac) prepared by electron bombardment[14] is assigned to the filling of $O_b$(vac).[64] As an estimate (Figure 7-b), half $O_b$(vac) ($\simeq 1.3\text{−}2.6\,10^{13}.\mathrm{cm}^{-2}$ if the $O_b$(vac) density $\simeq 0.05 - 0.1$ ML $O_b$[31,41,65] with 1 ML=$5.2\,10^{14}.\mathrm{cm}^{-2}$) are healed after 0.05 L $O_2$ ($1.8\,10^{13}$ $O_2.\mathrm{cm}^{-2}$); this corresponds to a sticking probability close to unity.[58] Therefore, the surface conductivity defined here requires the presence of oxygen vacancies, apparently at odds with the common postulate of the independence of the spectroscopic signature of excess electrons from their source. The point will be addressed in the discussion.

At 100 K, in a second step, after the steep decrease that parallels that of plasmons (Figure 7-b), the slow evolution of the BGS intensity once $O_b$(vac) are filled (beyond the blue vertical dashed line, Figure 7-b) is associated to charge transfer from $Ti_{int}$ to adsorbed oxygen;[14] a similar two-step behavior is observed at $T = 300$ K (on each side of the red dashed line, Figure 7-b) but shifted in exposure. Indeed, out-diffusion of $Ti_{int}$ triggered by O-adsorption is ruled out at room-temperature and a fortiori below.[66,67] Now arises the question of the location of the $Ti_{int}$ at the origin of the charges. Consistently with their absence in photodiffraction patterns,[10] $Ti_{int}$ are expected to be repelled beyond the third layer by $O_b$(vac).[31] However, when $Ti_{int}$ are located between the 4th and 5th Ti layers, their excess charges are predicted to populate their vicinity but also the subsurface;[68] this suggests to call "surface $Ti_{int}$" those Ti which participate in the subsurface charge. Conversely, BGS not healed by $O_2$ in the absence of $Ti_{int}$ diffusion, stem from what can be called "bulk $Ti_{int}$" (stroke symbols in Figure 7-b) that are found at a depth of $\simeq 30$ Å and beyond, as estimated by EELS probing depth (SI of Reference 14).

The relative contributions of $O_b$(vac) and "surface $Ti_{int}$" to the surface charge density $n_S$ can be quantified by associating their healing to each side of the blue (100 K) and red (300 K) vertical dashed lines in Figure 7, via $(\Omega_{gs,S}[O_b(\mathrm{vac})]/\Omega_{gs,S}[Ti_{int}])^2 \simeq n_S[O_b(\mathrm{vac})]/n_S[Ti_{int}] \simeq 1.5$ ($\simeq$ 60 %/40 %) at 100 K and $\simeq 3$ ($\simeq$ 75 %/25 %) at 300 K. Those values match other analyzes of similar sputtered/annealed surfaces (at 300 K: 66 %/34 %,[15] 78 %/22 %,[69] 65 %/35 %[65] and 62 %/38 %[70]), which nicely supports the present analysis. This agreement does not however prove that this ratio converges towards a value corresponding to an intrinsic parameter of the surface region of the titanium oxide. It simply expresses that a given mode of preparation (here sputtering/annealing) is rather reproducible. Indeed, the $O_b$(vac)/$Ti_{int}$ proportion

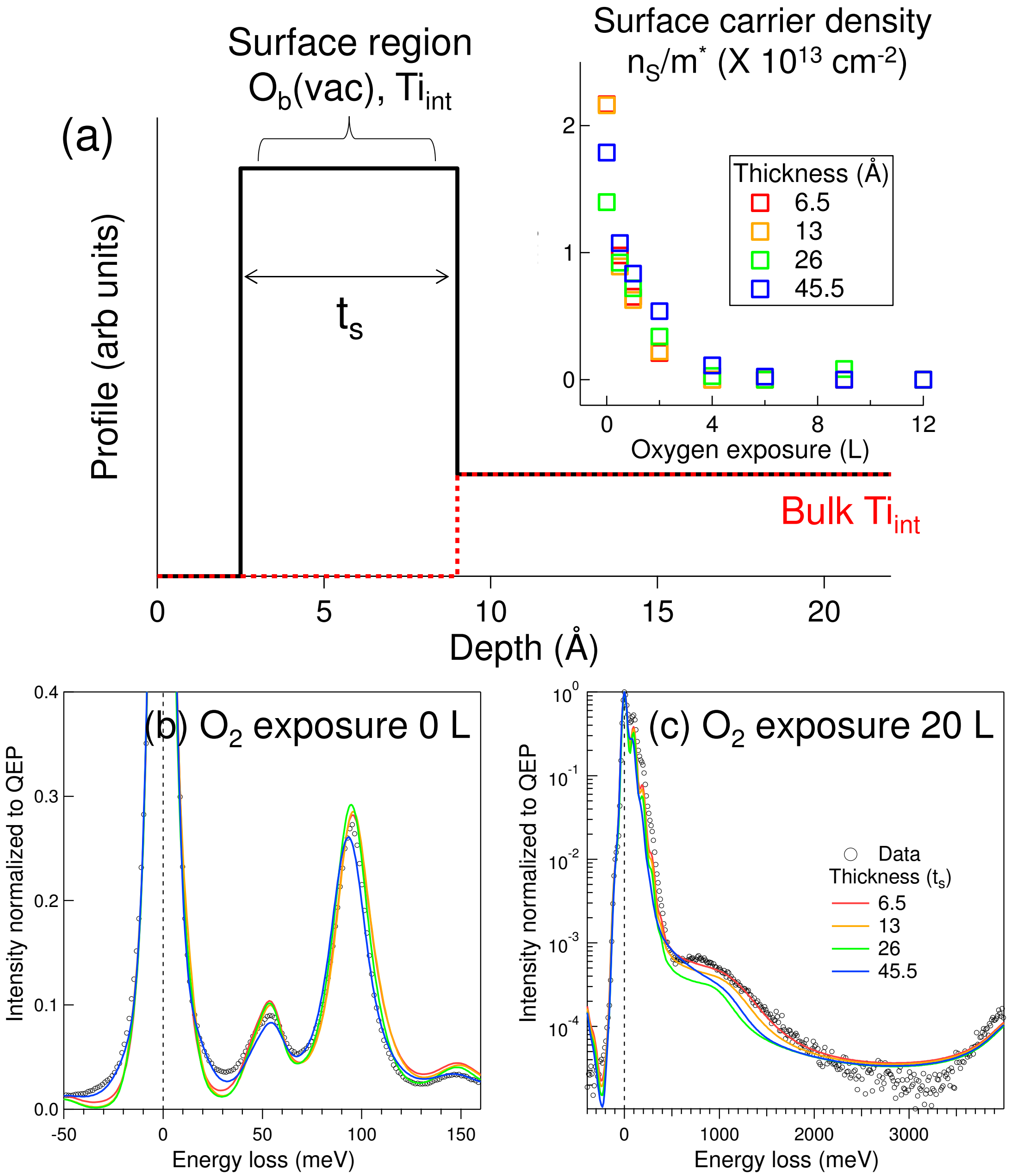

Figure 6: Carrier profile in the surface region of $TiO_2(110)$: (a) schematic profile of excess electron concentrations for reduced (black full line, $t_S = 6.5$ Å, see text) and oxygen exposed surface (red dotted line); (b) impact of the subsurface layer thickness $t_S$ on the best achievable fits on HREELS (exposure 0 L of $O_2$) and (c) EELS (exposure 20 L of $O_2$) recorded at 300 K with the incident plane perpendicular to the c-axis of $TiO_2$ - The inset of (a) shows the surface carrier density $n_S/m^*_\perp \propto \omega^2_{P,S} t_S$ as a function of $O_2$ exposure obtained from (a) and (b) fits of loss spectra for different thicknesses $t_s$.

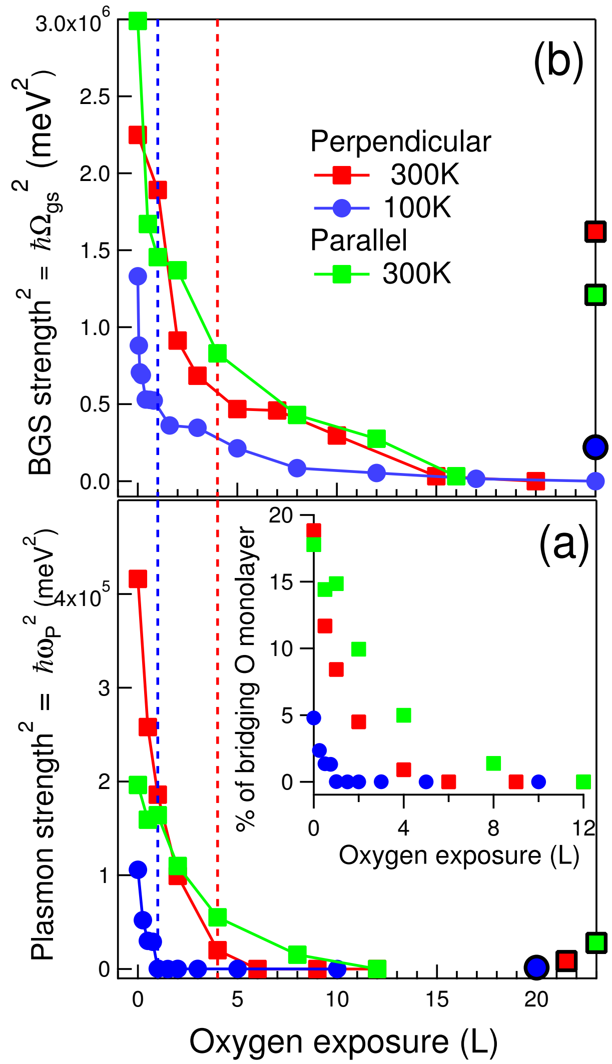

Figure 7: Evolution upon $O_2$ exposure at 300 K (red, green) and 100 K (blue) of (a) the surface plasmon strength $\omega^2_{P,S}$ and (b) the surface band gap strength $\Omega^2_{gs,S}$. Values are obtained from fits of (HR)EELS spectra with a scattering plane perpendicular (red/blue) or parallel (green) to the c-axis. The stroke symbols in figures a,b correspond to bulk values $\Omega^2_{gs,B}$, and $\omega^2_{P,B}$. Notably, the values at 300 K (green and red stroke symbols) correspond to the enhanced QEP shoulders (Figure 3-d,e). The dotted lines are guides for the eyes (see text). The inset of figure b is the surface carrier density $n_S = m^* t_S \omega^2_{P,S} \epsilon_0 m_e / e^2$ expressed in terms of bridging oxygen monolayer.

depends very much on the preparation process[70] since, at the two extremes, each species can be obtained alone.[14] Finally, an estimate of $O_b$(vac) $\simeq 10$ % $O_b$ (inset of Figure 7-a) in fair agreement with common values[2] is obtained by taking $n_S = 2.10^{14}$ cm$^{-2}$ (Table S1; $m^*_\perp = 10$), $n_S[O_b(\mathrm{vac})]/n_S[\mathrm{Ti}_{int}] \simeq 2:1$ and assuming two electrons per $O_b$(vac).

### 3.2.2 Bulk dielectric behavior

Treating $TiO_2$ as a regular n-type semiconductor, the bulk defect donor concentration $N_D$ (density of carriers represented in Figure 6-a), the donor defect ($E_D$) and Fermi ($E_F$) levels relative to the bottom of the conduction band $E_C$ can be estimated[71] in a model of a parabolic density of conduction states (see Section S2 for details). ($E_D$ differs from the BGS energy *i.e.* a fast optical excitation without relaxation of phonons around excess electrons). Assuming a freezing regime at 100 K and an exhaustion regime at 300 K in line with transport studies,[44,72] the present $n_B/m^*$ values lead to $E_C$ close to $E_D$ ($E_C - E_D = 30 \pm 10$ meV for $m^* = 10$). This matches the activation energy of carriers determined at similar temperatures by resistivity ($20 - 30$ meV[73] and 28 meV[74]), Hall effect (25 meV[44]) and levels derived by modeling conductivity and Hall mobility ($E_C - E_D = 40 - 60$ meV[75] or 25 meV[72]). The exhaustion regime at 300 K sets also $E_F$[71] close to $E_C$ ($E_C - E_F \simeq 64 \pm 5$ meV with $m^* = 10$), as seen by inverse photoemission[76] and STM.[77] The bulk carrier damping $\Gamma_{P,B}$ yields an electron drift mobility $\mu_B > 6$ cm$^2$.V.s$^{-1}$ (for $m^* = 10$) larger than Hall determinations ($\mu_H = 0.8$ cm$^2$.V.s$^{-1}$),[44,75] but drift and Hall mobility may differ in tetragonal symmetry.[44,78] Finally,[32] the donor concentration $N_D = n_B(300K)$ leads to a degree of reduction $x \simeq 10^{-3}$ in $TiO_{2-x}$ consistent with $p_{O_2}$-defect diagrams[79] ($x \simeq 10^{-3}$ at $p_{O_2} = 10^{-8}$ Pa and $T = 1273$ K), electric and Hall measurements on rutile annealed in similar conditions[44] and values commonly used in surface analysis.[58]

More qualitatively, but at specific depths, direct estimates of carrier density are derived from plasmon and BGS strengths obtained after strong $O_2$ exposure (Figure 7, stroke symbols) by assuming similar surface and bulk BGS transition probabilities for excess electrons. The $\mathrm{Ti}_{int}$-related bulk BGS oscillator strength leads to $(\Omega_{gs,S}[\mathrm{O}_b(\mathrm{vac})]/\Omega_{gs,B}[\mathrm{Ti}_{int}])^2 \simeq n_S[\mathrm{O}_b(\mathrm{vac})]/n_B[\mathrm{Ti}_{int}]d_{BGS} \simeq 1.5-3.5$ (dashed line limits and stroke symbols in Figure 7-b), where $d_{BGS} \simeq 30$ Å is the EELS probing depth at BGS energy (SI of Reference 14). By comparison to $n_S[\mathrm{O}_b(\mathrm{vac}) + \mathrm{Ti}_{int}(\mathrm{surface})]/n_B[\mathrm{Ti}_{int}]t_S \simeq 50$ (Table S1; $t_S = 6.5$ Å), this sets a concentration of $\mathrm{Ti}_{int}$-related excess electrons in the first layers one order of magnitude larger than $n_B$. The bulk $\mathrm{Ti}_{int}$-related plasmon oscillator strength (Figure 7-a) samples deeper layers ($d_{plasmon} \simeq 60$ Å, SI of Reference 14). It leads to $n_S[\mathrm{O}_b(\mathrm{vac})]/n_B[\mathrm{Ti}_{int}]d_{plasmon} \simeq 7-70$ which, as expected, is of the order of magnitude of $n_B$. A gradual change in density is likely closer to reality than the abrupt profile used in the fitting process (Figure 6-a). However, the latter should be kept as it is as a more realistic shape would introduce too many parameters to allow reliable estimates. Overall, the charge density profile chosen to model (HR)EELS data (Figure 6-a) is validated *a posteriori* by the consistency of the obtained parameters.

### 3.2.3 Band bending

To explain the high electron density of the R-$\mathrm{TiO}_2(110)$ subsurface (Figure 6-a and Table S1), two scenarios can *a priori* be invoked (i) either a downwards band bending and an accumulation layer due to surface defect states at the native surface or (ii) a spreading of excess electrons dictated by the surface/subsurface electrostatic potential.[14] In a classical n-type semiconductor, the charge transfer between bulk and surface states/defects is at the origin of space-charge layer and band bending[71,80] (Figure 8-a). The Debye length $L_D = \sqrt{2V_{bb}\epsilon_0\epsilon(0)/en_B}$, over which screening by bulk carriers is effective, gives an estimate of the spatial extension of the band bending of amplitude $V_{bb}$. As a surface of such semiconductor with donor defects inducing an accumulation layer (Figure 8-a), R-$\mathrm{TiO}_2(110)$ undergoes an upwards change in band bending $\Delta V_{bb}$ (energy separation between the valence band maximum and the Fermi level $\Delta(E_V - E_F)$) of $\simeq -0.4$ eV[9,27] upon exposure to electronegative $O_2$ molecules[9,27,70,81] (Figure 8-b). Assuming that $-V_{bb} = \Delta V_{bb} = -0.4$ eV[9,27] (see Section S3), *i.e.*, that flat bands are recovered at the end of exposure, one finds $L_D \simeq 80$ Å for $\epsilon(\omega = 0) = 85$ and $n_B = 6.1\,10^{19}$ cm$^{-3}$ at $T = 300$ K if $m^* \simeq 10$ (Table S1). However, the associated total screening charge $Q_s \simeq n_B L_D \simeq 4.9\,10^{13}$ cm$^{-2}$ is smaller than the surface carrier density found herein ($n_S \simeq 2\,10^{14}$ cm$^{-2}$; $m^* = 10$) while $L_D$ is much larger than the thickness $t_S = 6.5$ Å of the electron-rich subsurface layer. Therefore, the classical picture of band bending is clearly not consistent with the present findings that favor polarons confined by the surface/subsurface electrostatic potential instead of a defect-induced accumulation layer.

In contrast to the rapid decrease in BGS intensity below 100 L of $O_2$, at least half the change in $\Delta V_{bb}$ determined by photoemission occurs at higher exposure (Figure 8-b),[9] which parallels the present evolution of $\Omega^2_{gs,S}$ and $\omega^2_{P,S}$ (Figure 7-a,b). Since measurements shown in Figure 8-b were performed at the onset (400 K) of the diffusion of $\mathrm{Ti}_{int}$,[66,67] the high exposure region of Figure 8-b corresponds to the diffusion of $\mathrm{Ti}_{int}$ to the surface. This discards $\mathrm{O}_b(\mathrm{vac})$ as the main cause of the band bending and proves instead a shared role of $\mathrm{O}_b(\mathrm{vac})$ and $\mathrm{Ti}_{int}$.

# 4 Discussion

The occurrence of surface conductivity was shown herein to require the presence of $\mathrm{O}_b(\mathrm{vac})$, since the conductivity disappears when $\mathrm{O}_b(\mathrm{vac})$ are filled by reaction with oxygen while $\mathrm{Ti}_{int}$-related excess electrons are still observed (Figures 7-a). This suggests considering the often

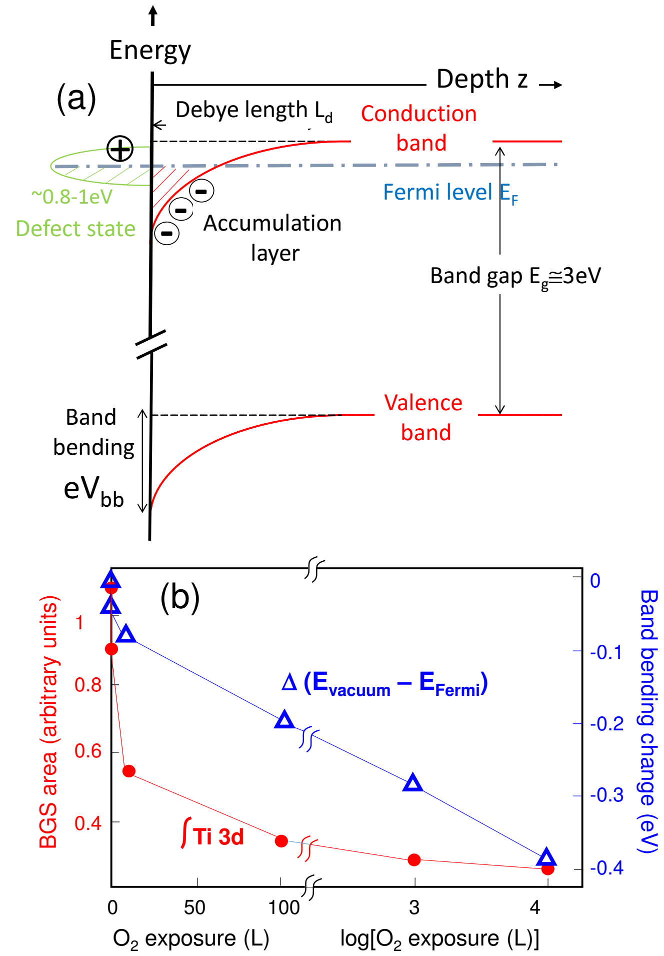

Figure 8: (a) Schematic band diagram for donor surface defects inducing an accumulation layer and a downward band bending in a classical n-type semiconductor. (b) Relative variation with $O_2$ exposure of the BGS intensity ($\int Ti(3d)$, red filled circles) and of band bending $\Delta(E_V - E_F)$ (open blue triangles) (after Reference 9) at the $TiO_2(110)$ surface. To better visualize the evolution of $\Delta(E_V - E_F)$ and of the BGS intensity, $O_2$ exposure is represented with a linear scale up to 100 L and a logarithmic scale above.

overlooked influence of the source of the excess electrons on their properties. The localization of excess electrons is generally assumed to depend only on electrostatics.[10,14,18,22,24,30,82] With regard to numerical simulations, both $O_b$(vac)[18,20] and $Ti_{int}$[68] were shown to give rise to excess charges on $Ti_{5c}$ in $1^{st}$, $2^{nd}$ and $3^{rd}$ layers with a dominant density on $Ti_{5c} - 2^{nd}$. However, it has been suggested that the presence of $Ti_{int}$ in subsurface layers induces, in relation to $O_b$(vac), an additional population of excess electrons which is at the origin of a specific reactivity of R-$TiO_2(110)$ with oxygen.[15] A direct proof of the perturbation of the location of excess electrons related to a given defect by the presence of another type of defect was given upon filling $O_b$(vac) by $O_bH$ groups;[41] an electron redistribution around surface $Ti_{6c} - 1^{st}$ bonded to $O_bH$ was evidenced by a decrease in the $O^+$ ESD yield from surface lattice $O^{2-}$ ions,[41] although the overall BGS intensity is not affected by the adsorbed proton.[41,65,82] The view is supported by the prediction that the excess electrons related to two neighboring $O_bH$ groups (common case), are localized on $Ti_{6c} - 1^{st}$ and $Ti_{5c} - 2^{nd}$ instead of $Ti_{5c} - 2^{nd}$ for a unique $O_bH$ group.[83] This result indicates, that insofar as, under ultra-high vacuum, the oxygen vacancies are gradually hydroxylated, the localization of the electrons in excess could vary during the duration of the experiments.

Also, surface reactions can be specifically associated with given types of defects. A catalytic cycle is predicted for the oxidation of CO in the presence of $Ti_{int}$ which do not diffuse but react via the released excess electrons,[84] which points to the above "surface $Ti_{int}$". The prediction is substantiated by the observation that CO oxidized on O-covered R-$TiO_2(110)$ (after $O_2$ pre-adsorption) releases excess electrons that are further healed by $O_2$ exposure.[70,85] On another side, those that are reminiscent of bulk-$Ti_{int}$ participate directly in many surface reactions via inward/outward diffusion,[27,58] as $O_2$ dissociation,[15,27] segregation of dopants,[86] deoxygenation of methanol,[87] decomposition of carboxylates.[88] Therefore, chemical activity appears to be very discriminating for differentiating point defects.

Overall, the similarity of the spectroscopic signatures of the excess electrons associated with either type of defects[14,18,22,30] hides very different realities, in particular the location of excess electrons and the way their properties are affected by the nature of the defects. The elusiveness of interstitials is a major obstacle here, as the properties of the surface therefore depend in part on species which may not be directly detected. Dilemmas relating to the specificity of sites and their interactions call for both experimental and theoretical studies dedicated to controlled populations of defects.

# 5 Conclusion

The dielectric behavior of the reduced rutile $TiO_2(110)$ was explored by HREELS. As a pivotal ingredient, the never directly observed carrier plasmon excitations were unambiguously featured by the broadening of the quasi-elastic peak (QEP) and its change in shape upon $O_2$ exposure. Previously used to explore deep surface layers, to distinguish $O_b$(vac) and $Ti_{int}$[14] and to highlight the double behavior of excess electrons,[32] HREELS identifies here each type of excitation and disentangles their role:

- Fits of the concomitant decrease upon $O_2$ exposure of BGS and QEP/phonon ratio could be obtained with a charge density profile involving a dead zone, electron rich three subsurface Ti layers (carrier concentration $n_S = 2.\,10^{14}$ cm$^{-2}$). Bulk concentration ($n_B = 6.1\,10^{19}$ cm$^{-3}$ or $x \simeq 0.001$ in $TiO_{2-x}$), Fermi ($E_C - E_F \simeq 64$ meV) and bulk donor ($E_C - E_D \simeq 30$ meV) levels agree with common estimates. The anisotropy of effective masses is lower at surface than in the bulk but electrons appear less mobile.
- Fits of the evolution of the BGS oscillator strength and Drude plasma frequency upon $O_2$ exposure distinguish excess electrons related to (i) $O_b$(vac), (ii) surface $Ti_{int}$, so defined as they contribute to the subsurface charge density and are healed by $O_2$ at 100 and 300 K in the absence of $Ti_{int}$ diffusion, and (iii) bulk $Ti_{int}$ still present after strong $O_2$ exposure. The concentration ratios of the different types of defects can be determined, but they appear contingent as they crucially depend on the surface preparation.
- The three categories of point defects have distinct properties. They all contribute to band bending but but each exhibits a specific chemical activity.

Finally, the present work evidences that the different types of defects, alone or by cross influences, shape the location and the properties of excess electrons, which makes it crucial to take into account the fact, often overlooked, that excess electrons do not behave independently of their source. Examples are the surface conductivity of the R-$TiO_2(110)$ surface which requires the presence of $O_b$(vac) (this work), the prediction that $Ti_{int}$ perturb the localization of excess electrons associated to $O_b$(vac)[15] and the specific localization of excess electrons entailed by surface hydroxyl groups with respect to $O_b$(vac).[41] This suggests going beyond the similarity of the physical fingerprints of the excess charges and to explore the defined configurations that results from either defects taken individually or controlled combinations of defects.

**Acknowledgement** The PhD thesis of J.L. was funded by the Chinese Scholarship Council.

# Supporting Information Available

Dielectric fits of loss spectra; Calculation of bulk dielectric properties; Band bending and photoemission.

# References

(1) Diebold, U. The surface science of titanium dioxide. *Surf. Sci. Rep.* **2003**, *48*,

53.

(2) Henderson, M. A. A surface science perspective on $TiO_2$ photocatalysis. *Surf. Sci. Rep.* **2011**, *66*, 185–297.

(3) Jupille, J.; Thornton, G. *Defects at oxide surfaces*; Springer: New York, 2015.

(4) Yin, W.-J.; Wen, B.; Zhou, C.; Selloni, A.; Liu, L. M. Excess electrons in reduced rutile and anatase $TiO_2$. *Surf. Sci. Rep.* **2018**, *73*, 58–82.

(5) Lun Pang, C.; Lindsay, R.; Thornton, G. Chemical reactions on rutile $TiO_2$(110). *Chem. Soc. Rev.* **2008**, *37*, 2328.

(6) Dohnálek, Z.; Lyubinetsky, I.; Rousseau, R. Thermally-driven processes on rutile $TiO_2$(110)-(1 × 1): A direct view at the atomic scale. *Prog. Surf. Sci.* **2010**, *85*, 161–205.

(7) Pang, C. L.; Lindsay, R.; Thornton, G. Structure of clean and adsorbate-covered single-crystal rutile $TiO_2$ surfaces. *Chem. Rev.* **2013**, *113*, 3887–3948.

(8) Henrich, V. E.; Dresselhaus, G.; Zeiger, H. J. Observation of two-dimensional phases associated with defect states on the surface of $TiO_2$. *Phys. Rev. Lett.* **1976**, *36*, 1335–1339.

(9) Kurtz, R.; Stockbauer, R.; Madey, T.; Román, E.; de Segovia, J. Synchrotron radiation studies of $H_2O$ adsorption on $TiO_2$. *Surf. Sci* **1989**, *218*, 178–200.

(10) Krüger, P.; Jupille, J.; Bourgeois, S.; Domenichini, B.; Verdini, A.; Floreano, L.; Morgante, A. Intrinsic nature of the excess electron distribution at the $TiO_2$(110) surface. *Phys. Rev. Lett.* **2012**, *108*, 126803.

(11) Yim, C. M.; Pang, C. L.; Thornton, G. Oxygen vacancy origin of the surface band-gap state of $TiO_2$(110). *Phys. Rev. Lett.* **2010**, *104*, 036806.

(12) Borghetti, P.; Meriggio, E.; Rousse, G.; Cabailh, G.; Lazzari, R.; Jupille, J. Photoemission fingerprints for structural identification of titanium dioxide surfaces. *J. Phys. Chem. Lett.* **2016**, *7*, 3223–3228.

(13) Epling, W. S.; Peden, C. H. F.; Henderson, M. A.; Diebold, U. Evidence for oxygen adatoms on $TiO_2$(110) resulting from $O_2$ dissociation at vacancy sites. *Surf. Sci.* **1998**, *412-413*, 333–343.

(14) Li, J.; Lazzari, R.; Chenot, S.; Jupille, J. Contributions of oxygen vacancies and titanium interstitials to band-gap states of reduced titania. *Phys. Rev. B* **2018**, *97*, 041403(R).

(15) Papageorgiou, A. C.; Beglitis, N. S.; Pang, C. L.; Teobaldi, G.; Cabailh, G.; Chen, Q.; Fisher, A. J.; Hofer, W. A.; Thornton, G. Charge traps and their effect on the surface properties of $TiO_2$(110). *Proc. Natl. Acad. Sci. USA* **2010**, *107*, 2391–2396.

(16) Chiesa, M.; Paganini, M.; Livraghi, S.; Giamello, E. Charge trapping in $TiO_2$ polymorphs as seen by Electron Paramagnetic Resonance spectroscopy. *Phys. Chem. Chem. Phys.* **2013**, *15*, 9435.

(17) Krüger, P.; Bourgeois, S.; Domenichini, B.; Magnan, H.; Chandesris, D.; Le Fèvre, P.; Flank, A. M.; Jupille, J.; Floreano, L.; Cossaro, A. et al. Defect states at the $TiO_2$(110) surface probed by resonant photoelectron diffraction. *Phys. Rev. Lett.* **2008**, *100*, 055501.

(18) Deskins, N. A.; Rousseau, R.; Dupuis, M. Localized electronic states from surface hydroxyls and polarons in $TiO_2$(110). *J. Phys. Chem. C* **2009**, *113*, 14583–14586.

(19) Finazzi, E.; Di Valentin, C.; Pacchioni, G. Nature of Ti interstitials in reduced bulk anatase and rutile $TiO_2$. *J. Phys. Chem. Lett.* **2009**, *113*, 3382–3385.

(20) Kowalski, P. M.; Camellone, M. F.; Nair, N. N.; Meyer, B.; Marx, D. Charge

localization dynamics induced by oxygen vacancies on the $TiO_2(110)$ surface. *Phys. Rev. Lett.* **2010**, *105*, 146405.

(21) Morgan, B. J.; Watson, G. W. Intrinsic n-type defect formation in $TiO_2$ : a comparison of rutile and anatase from GGA+ U calculations. *J. Phys. Chem. C* **2010**, *114*, 2321–2328.

(22) Janotti, A.; Franchini, C.; Varley, J. B.; Kresse, G.; Van de Walle, C. G. Dual behavior of excess electrons in rutile $TiO_2$. *Phys. Status Solidi (RRL)* **2013**, *7*, 199–203.

(23) Deák, P.; Aradi, B.; Frauenheim, T. Quantitative theory of the oxygen vacancy and carrier self-trapping in bulk $TiO_2$. *Phys. Rev. B* **2012**, *86*, 195206.

(24) Moses, P. G.; Janotti, A.; Franchini, C.; Kresse, G.; Van de Walle, C. G. Donor defects and small polarons on the $TiO_2(110)$ surface. *J. Appl. Phys.* **2016**, *119*, 181503.

(25) Panayotov, D. A.; Yates, J. T. n-type doping of $TiO_2$ with atomic hydrogen-observation of the production of conduction band electrons by infrared spectroscopy. *Chem. Phys. Lett.* **2007**, *436*, 204 – 208.

(26) Sezen, H.; Buchholz, M.; Nefedov, A.; Natzeck, C.; Heissler, S.; Di Valentin, C.; Wöll, C. Probing electrons in $TiO_2$ polaronic trap states by IR-absorption: Evidence for the existence of hydrogenic states. *Science Reports* **2014**, *4*, 3808.

(27) Wendt, S.; Sprunger, P. T.; Lira, E.; Madsen, G. K. H.; Li, Z.; Hansen, J. O.; Matthiesen, J.; Blekinge-Rasmussen, A.; Laegsgaard, E.; Hammer, B. et al. The role of interstitial sites in the Ti3d defect state in the band gap of titania. *Science* **2008**, *320*, 1755–1759.

(28) Wendt, S.; Bechstein, R.; Porsgaard, S.; Lira, E.; Hansen, J. O.; Huo, P.; Li, Z.; Hammer, B.; Besenbacher, F. Comment on "Oxygen vacancy origin of the surface band-gap state of $TiO_2(110)$". *Phys. Rev. Lett.* **2010**, *104*, 259703.

(29) Yim, C. M.; Pang, C. L.; Thornton, G. Reply on comment on "Oxygen vacancy origin of the surface band-gap state of $TiO_2(110)$". *Phys. Rev. Lett.* **2010**, *104*, 259704.

(30) Albaret, T.; Finocchi, F.; Noguera, C.; De Vita, A. First-principles study of the $TiO_2(110)$ surface reduction upon Na adsorption. *Phys. Rev. B* **2001**, *65*, 035402.

(31) Yoon, Y.; Du, Y.; Garcia, J. C.; Zhu, Z.; Wang, Z.-T.; Petrik, N. G.; Kimmel, G. A.; Dohnalek, Z.; Henderson, M. A.; Rousseau, R. et al. Anticorrelation between surface and subsurface point defects and the impact on the redox chemistry of $TiO_2(110)$. *ChemPhysChem* **2015**, *16*, 313–321.

(32) Li, J.; Chenot, S.; Jupille, J.; Lazzari, R. Dual behavior or coexistence of trapped and free states in reducible rutile $TiO_2$. *Phys Rev B* **2020**, *102*, 081401(R).

(33) Ibach, H.; Mills, D. L. In *Electron Energy Loss Spectroscopy and Surface Vibrations*; Inc., A. P., Ed.; Academic Press Inc.: New York, 1982.

(34) Lucas, A. A.; Sunjić, M. Fast-electron spectroscopy of collective excitations in solids. *Prog. Surf. Sci.* **1972**, *2*, 75–137.

(35) Evans, E.; Mills, D. L. Theory of inelastic scattering of slow electrons by long-wavelength surface of optical phonons: multiphonon processes. *Phys. Rev. B* **1973**, *7*, 853–868.

(36) Mills, D. L. The scattering of low energy electrons by electric field fluctuations near crystal surfaces. *Surf. Sci.* **1975**, *48*, 59–79.

(37) Lambin, P.; Vigneron, J. P.; Lucas, A. A. Electron-energy-loss spectroscopy of multilayered materials: theoretical aspects and study of interface optical phonons in

semiconductor superlattices. *Phys. Rev. B* **1985**, *32*, 8203–8215.

(38) Cox, P. A.; Edgell, R. G.; Eriksen, S.; Flavell, W. R. The high resolution electron energy loss spectrum of $TiO_2(110)$. *J. Electron. Spectrosc. and Relat. Phenom.* **1986**, *39*, 117–126.

(39) Ibach, H. Optical surface phonons in zinc oxide detected by slow-electron spectroscopy. *Phys. Rev. Lett.* **1970**, *24*, 1416–1418.

(40) Knotek, M. L.; Feibelman, P. J. Ion desorption by core-hole Auger decay. *Phys. Rev. Lett.* **1978**, *40*, 964–967.

(41) Zhang, Z.; Cao, K.; Yates, J. T. Defect-electron spreading on the $TiO_2(110)$ semiconductor surface by water adsorption. *J. Phys. Chem. Lett.* **2013**, *4*, 674–679.

(42) Gervais, F.; Piriou, B. Temperature dependence of transverse and longitudinal optic modes in $TiO_2$ (rutile). *Phys. Rev. B* **1974**, *10*, 1642–1654.

(43) Schöche, D.; Hofmann, T.; Korlacki, R.; Tiwald, T.; Schubert, M. Infrared dielectric anisotropy and phonon modes of rutile $TiO_2$. *J. Appl. Phys.* **2013**, *113*, 164102.

(44) Yagi, E.; Hasiguti, R. R.; Aono, M. Electronic conduction above 4 K of slightly reduced oxygen-deficient rutile $TiO_{2-x}$. *Phys. Rev. B* **1996**, *54*, 7945–7956.

(45) Baumard, J. F.; Gervais, F. Plasmon and polar optical phonons in reduced rutile $TiO_2$. *Phys. Rev. B* **1977**, *15*, 2316–2323.

(46) Hendry, E.; Wang, F.; Shan, J.; Heinz, T. F.; Bonn, M. Electron transport in $TiO_2$ probed by THz time-domain spectroscopy. *Phys. Rev. B* **2004**, *69*, 081101(R).

(47) Rocker, G.; Schaefer, J. A.; Göpel, W. Localized and delocalized vibrations on $TiO_2(110)$ studied by high-resolution electron-energy-loss spectroscopy. *Phys. Rev. B* **1984**, *30*, 3704–3708.

(48) Eriksen, S.; Egdell, R. G. Electronic excitations at oxygen deficient $TiO_2(110)$ surfaces: a study by EELS. *Surf. Sci.* **1987**, *180*, 263–278.

(49) Lazzari, R.; Li, J.; Jupille, J. Dielectric study of the interplay between charge carriers and electron energy losses in reduced titanium dioxide. *Phys. Rev. B* **2018**, *98*, 075432.

(50) Lazzari, R.; Li, J.; Jupille, J. Spectral restoration in reflection energy electron loss spectroscopy based on iterative semi-blind Lucy-Richardson algorithm applied to rutile surfaces. *Rev. Sci. Instrum.* **2015**, *86*, 013906.

(51) http://www.lktech.com/products/lk2000.php,.

(52) Kesmodel, L. New high resolution electron spectrometer for surface vibrational analysis. *J. Vac. Sci. Technol. A* **1983**, *1*, 1456–1460.

(53) Lee, J.; Zhang, Z.; Yates, J. T. Electron-stimulated positive-ion desorption caused by charge transfer from adsorbate to substrate: oxygen adsorbed on $TiO_2(110)$. *Phys. Rev. B* **2009**, *79*, 081408.

(54) Henderson, M. A.; Epling, W. S.; Peden, C. H. F.; Perkins, C. L. Insights into photoexcited electron scavenging processes on $TiO_2$ obtained from studies of the reaction of $O_2$ with OH groups adsorbed at electronic defects on $TiO_2$ (110). *J. Phys. Chem. B* **2003**, *107*, 534–545.

(55) Lucas, A. A.; Vigneron, J. P. Theory of electron energy loss spectroscopy from surfaces of anisotropic materials. *Solid. Stat. Commun.* **1984**, *49*, 327–330.

(56) http://www.physik.de/mateck.

(57) Ibach, H. *Electron Energy Loss Spectrometers: The technology of high performance*; Springer-Verlag, 1991.

(58) Henderson, M. A.; Epling, W. S.; Perkins, C. L.; Peden, C. H. F.;

Diebold, U. Interaction of molecular oxygen with the vacuum-annealed $TiO_2(110)$ surface: molecular and dissociative channels. *J. Phys. Chem. B* **1999**, *103*, 5328–5337.

(59) Cox, P. A.; Flavell, W. R.; Williams, A. A.; Egdell, R. G. Application of Fourier transform techniques to deconvolution of HREELS spectra. *Surf. Sci.* **1985**, *152-153*, 784–790.

(60) Pascual, J.; Camassel, J.; Mathieu, H. Fine structure of the intrinsic absorption edge to $TiO_2$. *Phys. Rev. B* **1978**, *18*, 5606–1614.

(61) Noguera, C. *Physics and Chemistry at Oxide Surfaces*; Cambridge University Press: Cambridge, 1995.

(62) Didier, F.; Jupille, J. Layer by layer growth mode of silver on magnesium oxide (100). *Surf. Sci.* **1994**, *307-309*, 587–590.

(63) Palik, E. D. *Handbook of Optical Constants of Solids*; Academic Press, 1985; Vol. 1-3.

(64) Sokolović, I.; Reticcioli, M.; Čalkovský, M.; Wagner, M.; Schmid, M.; Franchini, C.; Diebold, U.; Setvín, M. Resolving the adsorption of molecular $O_2$ on the rutile $TiO_2(110)$ surface by noncontact atomic force microscopy. *Proceedings of the National Academy of Sciences* **2020**, *117*, 14827–14837.

(65) Walle, L. E.; Borg, A.; Uvdal, P.; Sandell, A. Probing the influence from residual Ti interstitials on water adsorption on $TiO_2(110)$. *Phys. Rev. B* **2012**, *86*, 205415.

(66) Zhang, Z.; Lee, J.; Yates, J. T.; Bechstein, R.; Lira, E.; Hansen, J.; Wendt, S.; Besenbacher, F. Unraveling the diffusion of bulk Ti interstitials in rutile $TiO_2(110)$ by monitoring their reaction with O adatoms. *J. Phys. Chem. C* **2010**, *114*, 3059–3062.

(67) Lira, E.; Wendt, S.; Huo, P.; Hansen, J. Ø.; Streber, R.; Porsgaard, S.; Wei, Y.; Bechstein, R.; Lægsgaard, E.; Besenbacher, F. The importance of bulk $Ti^{3+}$ defects in the oxygen chemistry on titania surfaces. *J. Am. Chem. Soc.* **2011**, *133*, 6529–6532.

(68) Morita, K.; Shibuya, T.; Yasuoka, K. Stability of excess electrons introduced by Ti interstitial in rutile $TiO_2(110)$ surface. *J. Phys. Chem. C* **2017**, *121*, 1602–1607.

(69) Du, Y.; Deskins, N. A.; Zhang, Z.; Dohnalek, Z.; Dupuis, M.; Lyubinetsky, I. Formation of O adatom pairs and charge transfer upon $O_2$ dissociation on reduced $TiO_2(110)$. *Phys. Chem. Chem. Phys.* **2010**, *12*, 6337–6344.

(70) Mitsuhara, K.; Okumura, H.; Visikovskiy, A.; Takizawa, M.; Kido, Y. The source of the Ti 3d defect state in the band gap of rutile titania (110) surfaces. *J. Chem. Phys.* **2012**, *136*, 124707.

(71) Mathieu, H. *Physique des semiconducteurs et des composants électroniques*; Masson, 1990.

(72) Acket, G. A.; Volger, J. On the electron mobility and the donor centres in reduced and Li doped rutile $TiO_2$. *Physica* **1966**, *32*, 1680–1692.

(73) Hollander, L.; Castro, P. L. Anisotropic conduction in nonstoichiometric rutile $TiO_2$. *Phys. Rev.* **1960**, *119*, 1882–1885.

(74) Iguchi, E.; Yajima, K.; Asahina, T.; Kanamori, Y. Resistivities of reduced rutile ($TiO_2$) from 300 K to exhaustion range. *J. Phys. Chem. Solids* **1974**, *35*, 597–599.

(75) Becker, J. H.; Hosler, W. R. Multiple-band conduction in n-type rutile $TiO_2$. *Phys. Rev.* **1965**, *137*, A1872–A1877.

(76) See, A. K.; Thayer, M.; Bartynski, R. A. Angle-resolved inverse-photoemission study of the nearly perfect $TiO_2(110)$

surface. *Phys. Rev. B* **1993**, *47*, 13722–13729.

(77) Setvin, M.; Franchini, C.; Hao, X.; Schmid, M.; Janotti, A.; Kaltak, M.; Van de Walle, G.; Kresse, G.; Diebold, U. Direct view at excess electrons in $TiO_2$ rutile and anatase. *Phys. Rev. Lett.* **2014**, *113*, 086402.

(78) Friedman, L. Hall effect in the polaron-band regime. *Phys. Rev. B.* **1963**, *131*, 2445–2456.

(79) Bak, T.; Nowotny, J.; Nowotny, M. K. Defect disorder of titanium dioxide. *J. Phys. Chem. B* **2006**, *110*, 21560–21567.

(80) Zhang, Z.; Yates, J. T. Band bending in semiconductors: chemical and physical consequences at surfaces and interfaces. *Chem. Rev.* **2012**, *112*, 5520–5551.

(81) Okazawa, T.; Kohyama, M.; Kido, Y. Electronic properties of Au nano-particles supported on stoichiometric and reduced $TiO_2$(110) substrates. *Surf. Sci.* **2006**, *600*, 4430–4437.

(82) Di Valentin, C.; Pacchioni, G.; Selloni, A. Electronic structure of defect states in hydroxylated and reduced rutile $TiO_2$ (110) surfaces. *Phys. Rev. Lett.* **2006**, *97*, 166803.

(83) Bonapasta, A. A.; Filippone, F.; Mattioli, G.; Alippi, P. Oxygen vacancies and OH species in rutile and anatase $TiO_2$ polymorphs. *Catal. Today* **2009**, *144*, 177 – 182.

(84) Yu, Y.-Y.; Gong, X.-Q. CO oxidation at rutile $TiO_2$(110): role of oxygen vacancies and titanium interstitials. *ACS Catalysis* **2015**, *5*, 2042–2050.

(85) Mitsuhara, K.; Okumura, H.; Visikovskiy, A.; Takizawa, M.; Kido, Y. Reaction of CO with O adatoms on rutile $TiO_2$(110) surfaces. *Chem. Phys. Lett.* **2011**, *513*, 84–87.

(86) Dupont, C.; Jupille, J.; Bourgeois, S.; Le Fèvre, P.; Verdini, A.; Floreano, L.; Domenichini, B. Substitution of titanium for magnesium ions at the surface of Mg-doped rutile. *J. Phys. Chem. C* **2020**, *124*, 11490–11498.

(87) Osmić, M.; Mohrhusen, L.; Al-Shamery, K. Bulk defect dependence of low-temperature partial oxidation of methanol and high-temperature hydrocarbon formation on rutile $TiO_2$(110). *J. Phys. Chem. C* **2019**, *123*, 7615–7626.

(88) Jensen, S. C.; Friend, C. M. The dynamic roles of interstitial and surface defects on oxidation and reduction reactions on titania. *Top. Catal.* **2013**, *56*, 1377–1388.

# Graphical TOC Entry